applied sciences

MDPI

Article

Characterization of Laser-Induced Photothermal Vibration for Young's Modulus Imaging toward Computer-Aided Detection

Katsuhiro Mikami [1,*], Akihiro Ishinoda [2] and Mitsutaka Nemoto [1]

[1] Faculty of Biology-Oriented Science and Technology, Kindai University, Wakayama 649-6493, Japan
[2] Graduate School of Biology-Oriented Science and Technology, Kindai University, Wakayama 649-6493, Japan
* Correspondence: kmikami@waka.kindai.ac.jp

Featured Application: Quantitative Young's modulus measurement of soft tissue tumors such as cancer cells with high spatial resolution.

Abstract: The stiffness of tumor cells has a significant influence on invasion and metastasis strategies. In this study, we developed a novel detection method, called laser resonance frequency analysis (L-RFA), for soft tissue tumors in physical oncology. In addition, we evaluated the characteristics of the laser-induced photo-thermal elastic wave (LIPTEW) obtained by L-RFA using agarose gels with different stiffnesses to simulate soft tissues. The LIPTEW diagnosis based on the audible wave range indicated a great potential too, which allows for the measurement of the stiffness of single cells while maintaining organ geometry. In particular, we observed vibrations with high spatial resolution of less than one-tenth of the laser irradiation spot size. From the obtained results, our proposed machine learning method achieved high accuracy and precision, with coefficient of determination R^2 = 0.950. The characterization of the LIPTEW on the L-RFA to predict single cell stiffness could be a milestone for future studies on physical oncology, soft-tissue tumor stiffness diagnoses, and medical imaging technologies.

Keywords: laser sensing; photothermal vibration; acoustic wave; Young's modulus

Citation: Mikami, K.; Ishinoda, A.; Nemoto, M. Characterization of Laser-Induced Photothermal Vibration for Young's Modulus Imaging toward Computer-Aided Detection. *Appl. Sci.* **2023**, *13*, 3639. https://doi.org/10.3390/app13063639

Academic Editor: Yu-Dong Zhang

Received: 16 February 2023
Revised: 6 March 2023
Accepted: 7 March 2023
Published: 13 March 2023

1. Introduction

In the 1970s, cancer research was dominated by molecular genetics and biochemistry [1]. However, in most solid tumors, malignant cells coexist with noncancerous tissue [2]. In addition, it is now clear that cancer growth and progression are associated with the microenvironmental and physical abnormalities of cancer cells and tumors [3–5]. Recently, physical oncology was proposed and applied to investigate soft tissue tumors, given that the hardness of tumor cells has a significant influence on invasion and metastasis strategies [6].Tumor cells differ in chemoresistance with respect to hardness, organ site, and metastatic performance [7–9]. For example, tumor cell hardness is critical relative to the surrounding cells because tumor cells may be stiffer than the surrounding tissue and may push the surrounding tissue away. Moreover, they may be softer than the surrounding tissue and develop in the interstitial space. Thus, cancer cells are characterized by heterogeneity within the tumor, ranging from physical and mechanical changes in the extracellular matrix (ECM) [10]. Macroscopic bio-stiffness evaluation schemes in vivo are widely used. The evaluation of the elastic modulus using ultrasound elastography has been conducted in clinical practice as a noninvasive method for the measured organ structures [11,12]. However, these techniques had a spatial resolution at the submillimeter scale and did not measure the elastic modulus of single cells wherein cell-to-cell interactions occur in the state of organ geometry.

By contrast, microscopic in vitro measurement methods at the single-cell level are common. For example, micropipette aspiration is the most classical approach for measuring

the mechanical properties of cells, cell nuclei, and tissues [13–15]. However, this technique has suffered from low throughput ranging from 180 s per cell, as indicated in studies published in the 1950s, [16] to 3.6 s per cell, as reported in the 1990s, [17]. Other methods, such as the magnetic tweezer assay [18], have been developed and utilized to measure DNA elasticity [19–22]. In the same tweezer assay, the optical tweezer method [23] using laser light was developed in 1968 and is still widely used. In a previous study, the stiffness of cells was reported by measuring the elastic modulus of single cells under optical radiation pressure using a technique referred to as optical stretcher [7]. While tweezer assays can evaluate cells such as red blood cells [24], they are not suitable for all cells [25]. Furthermore, these techniques cannot be evaluated in organ geometry because of their approach to single cells.

Atomic force microscope (AFM) has been utilized as a technique for microscopic cellular-level elasticity mapping while preserving organ geometry [26–28]. Using AFM on normal and malignant human breast biopsies, Plodinec et al. found that in late-stage cancers there was more softening in the center and an increase in stiffness toward the periphery with sclerosis of the tumor stroma [29]. This study is a clear example in which elastic modulus mapping provided very effective information. However, methods to assess mechanical properties at the single-cell level, including AFM, require high-precision instrumentation and specialized training. Hopefully, these challenges can be overcome to assess cellular response non-destructively and continuously in situ [30].

Recently, laser-induced thermoelastic waves were studied as a diagnostic technique referred to as laser resonance frequency analysis (L-RFA) for the initial stability of orthopedic implant installations [31–33]. The principle of L-RFA is based on the measurement of the laser-induced photothermal elastic wave (LIPTEW) on implants such as pedicle screws and acetabular cups. The LIPTEW can lead to resonant vibration, which consists of an audible frequency region and employs the same scheme as the hammering test used for the concrete walls of tunnels and fastening bolts of bridges [34,35]. The LIPTEW can provide forced oscillation on the sample surface, and the behavior reveals surface mechanical properties, as is achieved by palpation. Photoacoustic imaging (PAI), which is based on the same LIPTEW principle as L-RFA, uses the penetration of laser radiation into the body to achieve a higher spatial resolution of imaging using ultrasound [36,37]. This imaging is achieved by transmitting a nanosecond laser pulse into the blood vessels and measuring the propagation of ultrasound waves induced by the absorption of laser pulses by hemoglobin in the blood. Therefore, PAI is based on a detection technique, and is a different scheme from the elastic modulus measurement categorized as elastography. Similarly, the acoustic tweezers method [38–41] uses ultrasound waves to measure hardness, but as with optical and magnetic tweezers, its single-cell approach makes it impossible to measure while maintaining organ geometry.

The L-RFAs conducted in previous studies were realized using high-power pulsed lasers. A sweep pulse excitation method was demonstrated, in which the repetition frequency of the laser pulse was used to realize a low average power evaluation [42,43]. In this new frequency-sweep pulse excitation method, L-RFA evaluation was demonstrated with a metal disk and a low laser power of several milliwatts [43]. Therefore, this L-RFA technique is applicable to the stiffness diagnoses of soft tissue tumors by palpation using LIPTEW. Using a laser as the excitation source, excitation energy can be transmitted into a single microscopic cell in the order of optical wavelengths in a non-contact, quantitative manner while maintaining the macroscopic structure of the organ shape. Combined with optical fiber transmission technology, the system can be mounted on an endoscope, and is therefore a less invasive in vivo measurement method.

In this study, we evaluated the characteristics of LIPTEW on agarose gels with different Young's moduli to simulate soft tissues toward single-cell hardness measurements while maintaining organ geometry. The results obtained from this study suggest that the machine learning-based analysis method for the prediction of the Young's modulus using L-RFA data can contribute to computer-aided detection (CADe).

The proposed evaluation method using L-RFA demonstrates significant potential as a critical measurement technique required in the process of physical oncology for the evaluation of cell stiffness while preserving the shape of the organ. This method allows for the realization of elastic modulus imaging techniques by performing two-dimensional (2D) scanning. When cancer diagnosis based on combined multiple data is a critical data point, tumor cell stiffness presented by L-RFA diagnostic techniques based on big data analysis is essential for CADe. The dependence of laser-induced elastic waves on the stiffness, spatial resolution in measurements, and data analysis performance based on machine learning, as proposed in this study, represents a performance milestone for future soft-tissue tumor stiffness diagnostic and stiffness imaging technologies.

The rest of the paper is arranged as follows. Section 2 describes the measurement and analysis method using L-RFA. Section 3 presents the results. Section 4 discusses the advantages of this method, and Section 5 presents the conclusions of our study.

2. Materials and Methods

For Young's modulus evaluation, samples with quantitatively adjusted mechanical properties, a stable experimental setup, and replicable experiments are required. In addition, it is essential to establish a machine learning scheme for uniformly analyzing the big data obtained. This section describes each detail incorporated to accomplish this study.

2.1. Experimental Samples

In this study, 11 types of agarose gels with different mass concentrations were prepared to determine the variations in the Young's modulus by adjusting the amount of agarose dissolved in water. The Young's modulus was determined by measuring the displacement and stress of the sample in a simple push-in test using a force gauge, as shown in Figure 1a,b. Figure 2 presents the dependence of the Young's modulus on the mass concentration of the agarose powder. In this study, measurements were performed in the Young's modulus range of approximately 0.04–2.3 MPa. These values cover the Young's moduli for organs such as the stomach, esophagus, small intestine, and large intestine [44]. To make uniform the influence of laser absorption and scattering due to different agarose concentrations, SiC powder with a particle size of 45 μm was uniformly applied on the sample surface layer.

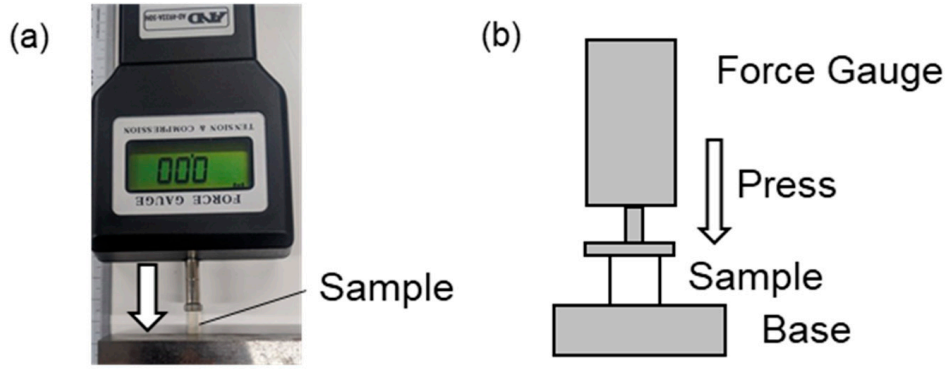

Figure 1. Experimental setup of simple push-in test to evaluate Young's modulus: (**a**) actual setup and (**b**) configuration diagram.

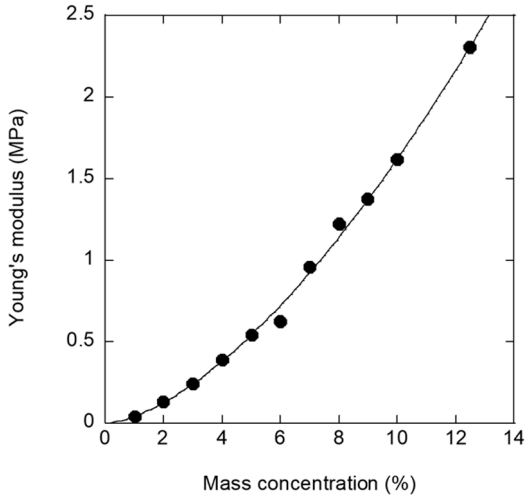

Figure 2. Young's modulus dependence of mass concentration of agarose.

2.2. Laser Irradiation Setting in L-RFA

Figure 3a,b show the experimental laser irradiation setup and configuration diagram in the L-RFA, respectively. A laser diode (LD) with a wavelength of 405 nm (Edmund Optics, #19-462) was used, and the LD repetition frequency was modulated by the transistor–transistor logic (TTL) signal as an external trigger from a functional generator. Ten measurements were performed for each agarose sample with different Young's moduli by L-RFA using sweep pulse excitation in a stepwise manner, as described in a previous study [41]. A plano-convex lens with a focal length of 100 mm was used to irradiate the samples. The average power of the laser irradiating the sample was approximately 25 mW, and the focal spot diameter was approximately 150 μm. The pulse width was dependent on the duty ratio of the TTL signal from the functional generator input to the LD. In this study, the pulse width was set such that half of the irradiation time interval corresponded to laser irradiation (50% duty ratio).

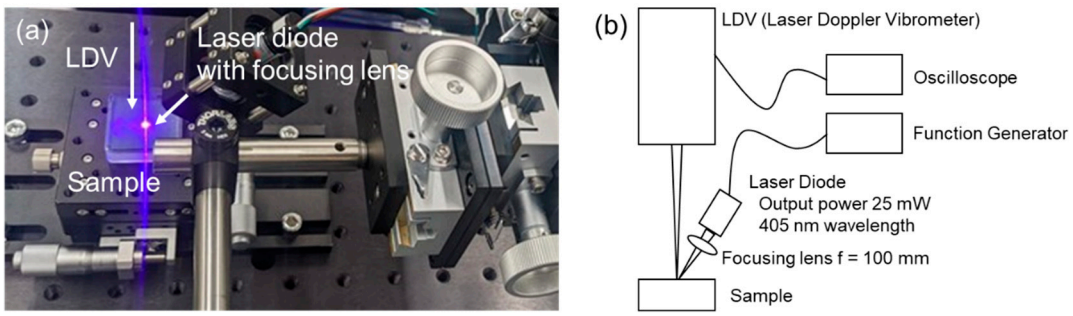

Figure 3. Experimental setup of L-RFA using sweep pulse excitation scheme: (**a**) actual irradiation setup and (**b**) configuration diagram.

The laser-induced photo-thermal elastic waves were measured using a single-point laser Doppler vibrometer (VibroOne, Polytec GmbH, Baden-Württemberg, Germany) and were recorded using an oscilloscope. The obtained measurement results were converted to a frequency spectrum using fast Fourier transform (FFT) analysis and smoothed based on a 50-point moving average to eliminate electrical spike noise.

The spatial resolution of the L-RFA was evaluated using a scanning laser Doppler vibrometer (PSV-500, Polytec GmbH; Baden-Württemberg, Germany). The average power of the laser irradiated on the sample was 25 mW, and the laser beam was defocused to a diameter of approximately 4 mm. The laser repetition frequency modulation was fixed at 924 Hz, and FFT analysis was performed on the results of eight measurements per sample.

2.3. Machine Learning-Based Analysis

Medical image analysis is one of the leading artificial intelligence (AI) applications in the medical field. Machine learning and deep learning are now being considered for adaptation for lesion detection, differential diagnosis, and region extraction. The dramatic improvement in AI performance has led to the proposal of the use of AI in clinical sites related with CT and MRI, especially by radiologists [45–50]. As an example of machine learning applied in tumor diagnosis related in this study, Solkov et al. achieved 94% accuracy by adapting Random Forests, which is an ensemble learning method used for classifications, to a bladder cancer diagnostic tool using AFM [51]. Thus, recent advances in machine learning technology have enabled the effective analysis of tumors.

However, Young's modulus is not a categorical but continuous value. Therefore, to obtain stiffness mapping and stiffness spectrum using numerical values in CADe by L-RFA as in cell evaluation using AFM, Young's modulus should be estimated using a regression method rather than using a simple classification problem such as stiffness or softness.

To realize CADe by analyzing the data obtained from the L-RFA, stiffness prediction was conducted based on machine learning using L-RFA data for agarose samples with different Young's moduli. The analysis was based on support vector regression (SVR), which was used in a previous study [52]. Three explanatory variables obtained from the vibrational frequency spectrum in the L-RFA were analyzed by SVR to predict the Young's modulus at the laser-irradiated area. Three types of explanatory variables, namely, the frequency center of gravity, intensity center of gravity, and peak intensity in the measured frequency region, were introduced into SVR as explanatory variables.

Support vector regression is an adaptation of the support vector machine (SVM) [53,54], which is a pattern recognition method, to regression, and can be adapted to nonlinear problems by incorporating a kernel function. In this study, we used a Gaussian kernel (RBF kernel), which generally exhibits a higher speed and accuracy. The basic principles of SVR and SVM are the same, and the regression performance by SVR leads to the classification performance in SVM. Therefore, SVR is the most optimal machine learning method that can generalize the performance of L-RFA hardness measurement, which will be considered as a benchmark.

The L-RFA data from 11 different agarose samples with different Young's moduli, as shown in Figure 2, were used to train the SVR used in this study. The hyperparameters required for learning SVR were determined with the least squares error in the grid search as follows: the insensitivity coefficient ε ranged from 2^{-20} to 2^{9}, the regularization coefficient C ranged from 2^{-10} to 2^{10}, and the RBF kernel function γ ranged from 2^{-15} to 2^{9}. The combination ($\varepsilon = 2^{-4}$, $C = 2^{3}$, and $\gamma = 2^{-2}$) was used in this analysis.

3. Results

The evaluation of Young's modulus requires the optimization of the evaluation conditions of the L-RFA. Moreover, it is necessary to understand how Young's modulus affects the results of the L-RFA evaluation. Thus, it is essential to evaluate the analysis and identify the factors that may affect model performance. In this section, we discuss the L-RFA conditions, present the accuracy of estimating Young's modulus evaluation via machine learning, and present the results of validating the spatial resolution for single-cell evaluation.

3.1. Influence of Laser Irradiation and Young's Modulus Parameters

In an L-RFA using the frequency sweep excitation method, the measurement time of each excitation frequency is a critical parameter. Therefore, to clarify the appropriate excitation conditions for agarose samples, measurements were conducted at different numbers of divisions in the frequency range of 1000–10,000 Hz with a measurement time of 2 s. The measurement frequency interval and each allocated time were determined by dividing equally the measurement time and measurement frequency band by the number of divisions. Figure 4 presents the vibration frequency spectra obtained for agarose with a

Young's modulus of 1.22 MPa for (a) 5 divisions (400 ms/div), (b) 10 divisions (200 ms/div), and (c) 40 divisions (50 ms/div).

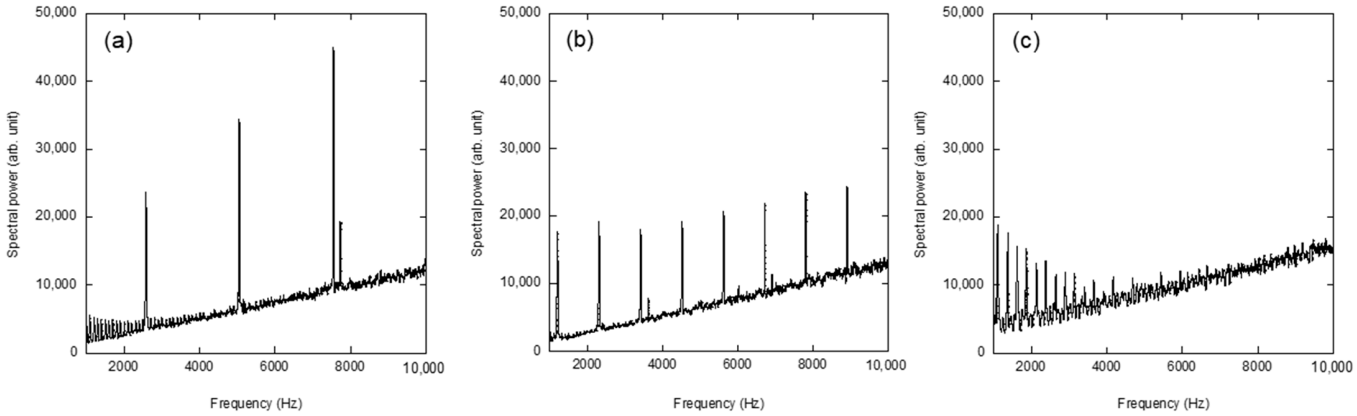

Figure 4. Laser-induced vibrational spectra of agarose with a Young's modulus of 1.22 MPa with respect to different numbers of divisions: (**a**) 5 divisions, (**b**) 10 divisions, and (**c**) 40 divisions.

When the measurement time allocated to one excitation frequency was shorter, it was difficult to average the noise components, thus resulting in a decrease in the signal-to-noise (S/N) ratio. Therefore, as shown in Figure 4a, when the number of divisions was small, data with a large S/N ratio were obtained; however, the amount of information obtained from the L-RFA was reduced due to the low excitation frequency. However, as shown in Figure 4c, when the number of divisions was excessively large, comb-shaped vibration peaks were not observed due to the decrease in the S/N ratio. In this experiment, we employed 10 divisions, as shown in Figure 4b, which clearly provide the results for multiple excitation frequencies.

In the sweep-frequency excitation method reported in previous studies, the main measurement principle was the adjustment of the repetition rate to the resonance frequency. Generally, the resonance frequency of soft materials used for vibration isolation is several tens of Hertz. Therefore, the vibration obtained at the excitation frequency in the measurement shown in Figure 4 was a vibration caused by forced excitation. Figures 5 and 6 present the L-RFA results for different Young's modulus values of (a) 0.042 MPa, (b) 0.76 MPa, and (c) 2.3 MPa in the same frequency range of 1000–10,000 Hz. The evaluation results revealed that at the frequencies where the forced vibration was utilized, the vibration intensity increased with the Young's modulus, as shown in Figure 5a,b. However, as shown in Figure 5c, a higher Young's modulus resulted in a higher noise level in the high-frequency band and a lower S/N ratio.

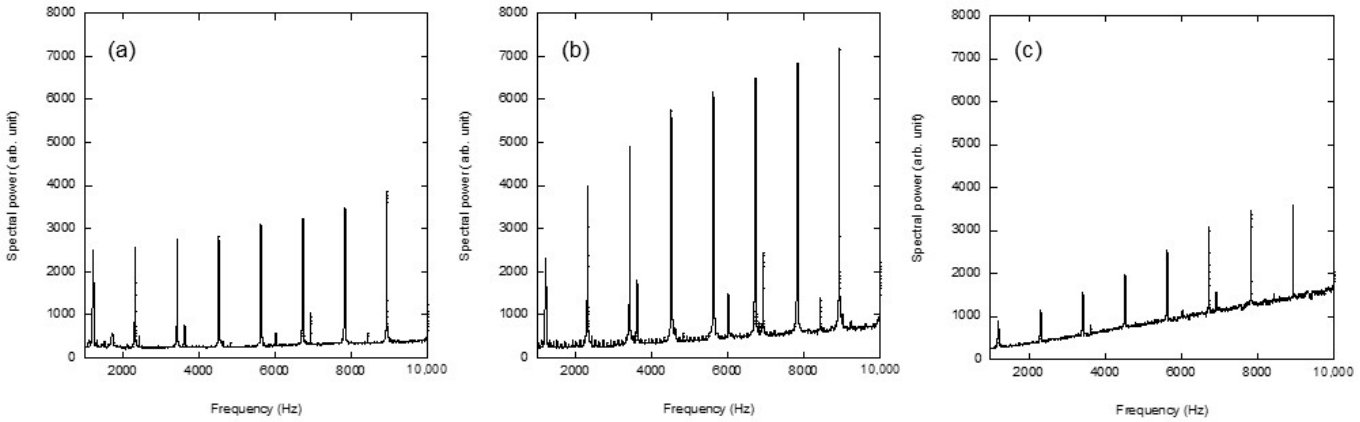

Figure 5. Laser-induced vibrational spectra of agarose with different Young's moduli of (**a**) 0.042 MPa, (**b**) 0.76 MPa, and (**c**) 2.3 MPa.

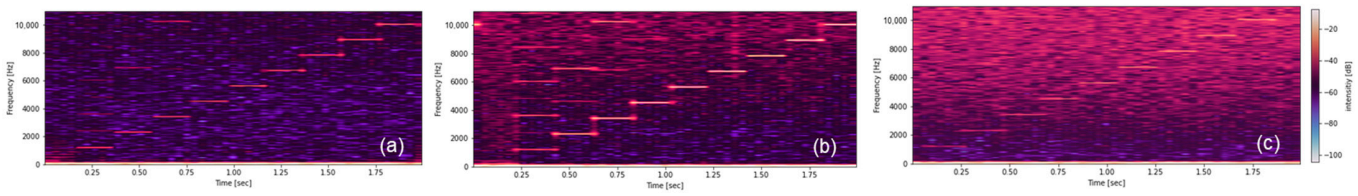

Figure 6. Laser-induced vibrational spectrogram of agarose with Young's moduli of (**a**) 0.042 MPa, (**b**) 0.76 MPa, and (**c**) 2.3 MPa.

To visualize the time-domain laser-induced vibrational spectra, Figure 6 presents spectrograms obtained by short-time FFT for different Young's moduli of (a) 0.042 MPa, (b) 0.76 MPa, and (c) 2.3 MPa. Figure 6a reveals that step-like forced excitation clearly occurred at a low Young's modulus. Figure 6b reveals that a higher Young's modulus caused higher-order vibration and forced excitation, and that the noise component was higher across the entire frequency band above the excitation frequency. As shown in Figure 6c, at a higher Young's modulus, the noise in the high-frequency band increased and the S/N ratio with forced excitation decreased.

3.2. Young's Modulus Prediction by Machine Learning Analysis

The final clinical application of this technology will be the stiffness measurement using L-RFA for in vivo soft tissue tumors by introducing optical fibers into an endoscope or other devices. Therefore, it is critical to obtain a more accurate Young's modulus from the obtained L-RFA results for application to CADe. To avoid learning extrapolation, the estimation performance was verified for nine agarose samples, excluding the largest and smallest datasets. Figure 7a presents the results of 10 measurements for each agarose sample used to train 100 data points and predict the 10 data points of a verified agarose sample. The variation in the estimated values for each Young's modulus was significantly large, and a sufficient estimation performance was not demonstrated. Moreover, Figure 7b presents the estimation results of one data point using the training data of 10 points by considering the average of the data measured at 10 points for each agarose sample. A comparison of the values is shown in Table 1. The coefficient of determination R^2 reached 0.950 and the mean squared error was 0.0322. The estimation results were close to an ideal approximate straight line ($y = x$), such that a linear approximation with a high coefficient of determination was obtained. This result indicates that although a large amount of training data is essential, averaging and sufficient data quality are more critical than the amount of data. Based on the results of this study, the Young's modulus estimation using SVR can be fully utilized.

Table 1. Prediction results of Young's modulus by machine learning-based analysis in Figure 7b.

	Actual Values in True and Predicted Young's Modulus								
True Young's modulus (MPa)	0.0424	0.129	0.241	0.388	0.539	0.627	0.957	1.22	1.37
Predicted Young's modulus (MPa)	0.0200	0.136	0.441	0.472	0.598	0.550	1.17	1.13	1.53

3.3. Spatial Resolution of the L-RFA

A high spatial resolution, comparable to that of a single cell in soft-tissue tumor stiffness measurement, is essential for physical oncology. The spatial resolution of L-RFA was evaluated using a scanning Doppler vibrometer to visualize the natural vibration due to LIPTEW. Figure 8 presents the evaluation conditions and results. As shown in Figure 8a, the sample surface was irradiated using an excitation laser at oblique incidence, and the center of the laser irradiation, as indicated by the blue dot in the figure, was measured. Figure 8b presents the measurement positions for a total of 235 points evaluated using the

scanning Doppler vibrometer. Figure 8c presents the evaluation results of the fundamental mode (924 Hz) and (d) second-harmonic mode (1848 Hz) for the agarose sample with a Young's modulus of 0.042 MPa. Figure 8e presents the results of the evaluation of the fundamental mode (924 Hz) and (f) the second harmonic mode (1848 Hz) for an agarose sample with a Young's modulus of 1.2 MPa. Due to oblique incidence, the laser irradiation spot was elliptical, and an oscillation range of approximately 2 mm was observed for an irradiation system of approximately 4 mm on average as shown in Figure 8c–e. This indicates that in the laser irradiation spot focused by the lens only a portion of the intensity, which was considered to exhibit a Gaussian distribution, oscillated. Moreover, when the laser irradiation scheme was optimized, the extremely high spatial resolution vibrational area, a small region with a diameter of less than one-tenth of the laser irradiation spot diameter, was provided as shown in Figure 8f. From the experimental results, it was necessary to utilize higher-order vibration modes for demonstrate high spatial resolution measurements. Also, materials with higher Young's modulus were easier to measure. In principle, the laser beam can be operated up to the abovementioned wave-length, and by scaling the results of this study it is expected that the laser beam can be operated to under several tens of micrometers, which would allow for a high spatial resolution (i.e., the size of a single cell).

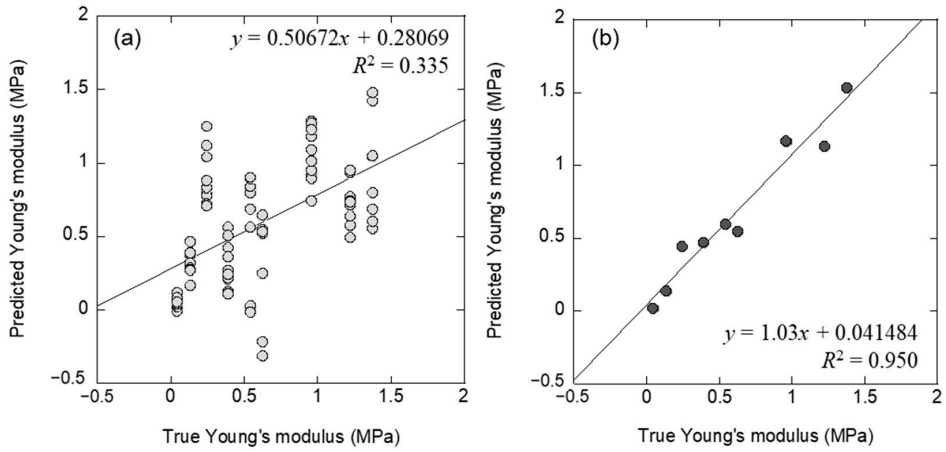

Figure 7. Prediction results of Young's moduli of agarose samples using machine learning-based analysis with (**a**) non-averaged data and (**b**) averaged data.

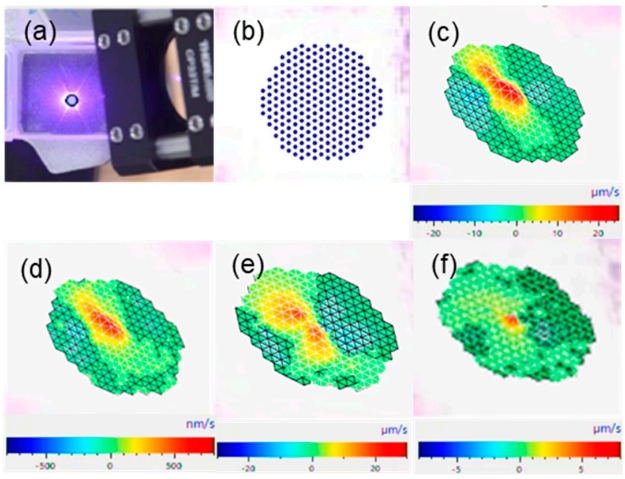

Figure 8. Evaluation settings of (**a**) overview and (**b**) scanning point of laser Doppler vibrometer, and behaviors of forced vibration obtained by L-RFA on agarose samples at different Young's moduli as (**c**) 924 Hz at 0.042 MPa, (**d**) 1848 Hz at 0.042 MPa, (**e**) 924 Hz at 1.2 MPa, and (**f**) 1848 Hz at 1.2 MPa, respectively.

4. Discussion

The L-RFA using the sweep-pulse excitation method is a technique used to search for resonance frequencies that match natural frequencies by adjusting the repetition rate of a low-power laser. Soft materials generally comprise frequencies that are several tens of Hertz lower than those of metals. However, in this study, forced vibrations of several kilohertz were considered. There are two reasons for this. First, soft materials exhibit lower Young's moduli than metals and dielectric materials, and are more readily subject to oscillation; thus, forced vibration can be more readily demonstrated. Second, forced vibration exhibits a lower decay time than resonance vibration, thus reducing the effect of changes in the excitation frequency during sweep-pulse excitation.

As shown in Figure 5, the L-RFA measurements revealed that the differences in Young's moduli influenced the vibration spectrum of LIPTEW. In a simple spring vibration model, the spring constant is proportional to the Young's modulus; therefore, materials with higher Young's moduli vibrate less readily. However, the vibration was higher for the agarose sample with a Young's modulus of 0.76 MPa, as shown in Figure 5b, when compared with that with a Young's modulus 0.042 MPa, as shown in Figure 5a. This indicates that the damping coefficient was higher due to the softer material. This can be seen in the spectrograms, as shown in Figure 6, where the forced excitation energy due to laser irradiation at 0.76 MPa (Figure 6b) was highly distributed into high order vibration modes with high attenuation coefficients, whereas the agarose sample at 0.042 MPa (Figure 6a) had less presence. The agarose sample with a Young's modulus of 0.042 MPa, as shown in Figure 6a, revealed that most of the vibrational energy was concentrated at the frequency of forced excitation. However, when the Young's modulus was further increased, the vibration intensity decreased, as shown in Figure 5c. The noise component in the high-frequency band increased, thus resulting in a decrease in the S/N ratio of the vibration spectrum. This would be influenced by the resonance frequency and the damping behavior was changed. The resonance frequency f_n presents the relationship expressed by Equation (1) between the spring constant k and Young's modulus E in the spring vibration model.

$$f_n \propto \sqrt{k} \propto \sqrt{E} \tag{1}$$

Thus, the agarose sample in Figure 6c should indicate a resonance frequency that was higher than that in Figure 6a by a factor of approximately 55. The vibration damping effect was greater at frequencies higher than the resonance frequency. Therefore, it was assumed that the sample with a high Young's modulus did not exhibit a sufficient damping effect in the high-frequency band, thus resulting in a lower S/N ratio.

The decrease in the S/N ratio at high Young's moduli has a negative influence because it prevents the acquisition of clear peaks in a simple spectral analysis. However, in the machine learning-based analysis used in this study, a high prediction accuracy was achieved by employing three types of multivariate nonlinear regression: center-of-gravity frequency, center-of-gravity intensity, and peak intensity. By introducing the center-of-gravity frequency and intensity as explanatory variables, the effect of increased noise in the high-frequency band at a high Young's modulus was reflected. In general, machine learning analysis should be based on a large amount of supervised data to obtain high accuracy. In this study, a higher accuracy was obtained by averaging the acquired data, as shown in Figure 7a, when compared with Figure 7b, training individual data. This suggests that sufficiently averaged data are required for soft materials because their morphologies are more unstable than those of metals and dielectrics, and the dispersion of the acquired data is larger. Additionally, it is more effective to select and combine the optimal explanatory variables among the multiple parameters. However, in this study, in the frequency range from 1000 to 10,000 Hz, the most accurate results were obtained using only the explanatory variables obtained from the entire frequency range described in Section 3.2, instead of using explanatory variables obtained by dividing the peaks at each peak of the sweep pulse excitation. This suggests that it is critical to evaluate changes in the noise intensity in the

high-frequency band due to differences in the Young's modulus over a wide range of low to high frequencies, instead of differences in individual peak intensities. In summary, the estimation of the Young's modulus of soft materials using machine learning requires a high-quality dataset that is sufficiently averaged for both the teacher and analysis. In future research, a detailed analysis of the vibration frequency spectra of soft materials obtained by L-RFA and the variance of the extracted explanatory variables will be conducted to provide quantitative data acquisition guidelines.

The high potential of stiffness measurement by L-RFA, when compared with other methods, is the evaluation of single cells in organ geometry. Therefore, the spatial resolution is the most critical parameter, and a few micrometers of a single cell should be achieved. In this study, the laser-induced thermoelastic excitation of soft materials by L-RFA was visualized using a scanning Doppler vibrometer, as described in Section 3.3. As a result, by analyzing the vibration of higher-order modes, the observation of vibrations of less than one-tenth of the laser irradiation spot size was demonstrated. This result demonstrates that a high spatial resolution can be achieved using higher-order modes, which are characteristics, in that only the central part of the laser beam with high light intensity oscillates. As shown in Figure 8d, even for the same higher-order mode, a high resolution was not achieved when the Young's modulus was low. This can be attributed to the propagation of vibrations without attenuation in the soft sample. Although this limits the realization of high spatial resolutions, it suggests that stiffness diagnoses can be conducted using information on vibration propagation. In particular, this method estimates stiffness from the attenuation of vibration intensity by varying the relative excitation and the laser irradiation position for vibration measurements and is expected to be used as CADe for abnormality detection to discriminate between hard tumors and normal soft tissues.

5. Conclusions

In this study, we evaluated the vibrational properties of agarose samples simulating soft-tissue tumors with different Young's moduli by L-RFA using a sweep pulse excitation method and validated a machine learning-based analysis method. It was found that the difference in Young's moduli is reflected in the difference in the vibration frequency spectra by utilizing the forced excitation generated by laser-induced elastic waves. Using the explanatory variables extracted from the L-RFA data, a machine learning-based analysis was performed to achieve a high Young's modulus prediction accuracy. Moreover, we found that it is critical to use more averaged data for the prediction of the Young's moduli of soft materials that are susceptible to disturbances. This stiffness evaluation by L-RFA revealed that a high spatial resolution below the irradiation spot size of the excitation laser can be obtained by observing higher-order vibration modes.

Diagnosis using the L-RFA technique was achieved by irradiating two laser beams, one to generate LIPTEW and the other to measure it. The laser beam can be easily and freely guided using an optical fiber and can be easily mounted on endoscopic instruments. This setup shows excellent potential to achieve in vivo measurements in situ. In addition, highly accuracy was demonstrated by the regression estimation of Young's modulus with a coefficient of determination R^2 of 0.950, using machine learning-based SVR analysis. The ability to handle continuous values, rather than a simple hard/soft classification problem, leads to stiffness mapping and the acquisition of stiffness spectra, which can make a significant contribution to CADe.

The stiffness measurement technique using L-RFA demonstrates significant potential for achieving cellular stiffness while preserving the shape of the organ. This method can facilitate the development of imaging techniques for elastic moduli by performing 2D scanning. In addition, machine learning-based analysis techniques for large amounts of L-RFA data are essential for CADe.

The LIPTEW generation and measurement technique in L-RFA is a quantitative, miniaturized, and precise assay of the physician's palpation technique, using a sweep pulse excitation scheme. The proposed scheme is noninvasive with very low laser power, and

thus, it allows for high cell viability measurements, which we expect to be studied in the future. In vitro and in vivo measurements of organ tumors using L-RFA will allow future studies to move into a more concrete verification phase for clinical use. Simultaneously, LIPTEW was generated by a 405 nm LD, which is a wavelength that is strongly absorbed on the organ surface. In the future, by using near-infrared wavelengths in the region of low absorption and through scattering on the living body, it will be possible to verify the approach for tumor cells that are located at a depth of several millimeters, which are not visible on the surface.

Additionally, in this demonstration, each measurement took 2 s. However, because the averaging of 10 measurements was necessary to improve the estimation accuracy by machine learning, a measurement time of 20 s per point is required. Therefore, the throughput is sufficiently high compared to the conventional pipette aspiration method, AFM, and optical tweezers. However, the throughput is comparable to the latest improved technique [17], which is an in vitro method. To clarify the superiority of the measurement method using L-RFA in the future, an improvement of the data cleansing technique is also necessary.

The demonstrated performance of L-RFA represents a milestone and can serve as a basis for future studies on physical oncology, soft-tissue tumor stiffness diagnoses, and medical imaging technologies.

Author Contributions: K.M. was responsible for all the procedures, laser system construction, data gathering, analysis, and writing of the manuscript. A.I. and M.N. were responsible for data analysis. All authors have read and agreed to the published version of the manuscript.

Funding: This work was supported by AMED (Grant Numbers JP20hm0102077h0001, JP21hm0102077h0002, and JP22hm0102077h0003).

Institutional Review Board Statement: Not applicable.

Informed Consent Statement: Not applicable.

Data Availability Statement: The datasets used and/or analysed during this study are available from the corresponding author on reasonable request.

Acknowledgments: The experiment using the scanning Doppler vibrometer was supported by Polytec Japan.

Conflicts of Interest: The authors declare no conflict of interest.

References

1. Bister, K. Discovery of oncogenes The advent of molecular cancer research. *Proc. Natl Acad. Sci. USA* **2015**, *112*, 15259–15260. [CrossRef]
2. McAllister, S.S.; Weinberg, R.A. Tumor-host interactions: A far-reaching relationship. *J. Clin. Oncol.* **2010**, *28*, 4022–4028. [CrossRef] [PubMed]
3. Cao, X.; Moeendarbary, E.; Isermann, P.; Davidson, P.M.; Wang, X.; Chen, M.B.; Burkart, A.K.; Lammerding, J.; Kamm, R.D.; Shenoy, V.B. A chemomechanical model for nuclear morphology and stresses during cell transendothelial migration. *Biophys. J.* **2016**, *111*, 1541–1552. [CrossRef] [PubMed]
4. Trimboli, A.J.; Cantemir-Stone, C.Z.; Li, F.; Wallace, J.A.; Merchant, A.; Creasap, N.; Thompson, J.C.; Caserta, E.; Wang, H.; Chong, J.L.; et al. Pten in stromal fibroblasts suppresses mammary epithelial tumours. *Nature* **2009**, *461*, 1084–1091. [CrossRef] [PubMed]
5. Friedl, P.; Alexander, S. Cancer invasion and the microenvironment: Plasticity and reciprocity. *Cell* **2011**, *147*, 992–1009. [CrossRef] [PubMed]
6. Jonietz, E. Mechanics: The force of cancer. *Nature* **2012**, *491*, S56–S57. [CrossRef]
7. Guck, J.; Schinkinger, S.; Lincoln, B.; Wottawah, F.; Ebert, S.; Romeyke, M.; Lenz, D.; Erickson, H.M.; Ananthakrishnan, R.; Mitchell, D.; et al. Optical Deformability as an Inherent Cell Marker for Testing Malignant Transformation and Metastatic Competence. *Biophys. J.* **2005**, *88*, 3689–3698. [CrossRef]
8. Baker, E.L.; Bonnecaze, R.T.; Zaman, M.H. Extracellular Matrix Stiffness and Architecture Govern Intracellular Rheology in Cancer. *Biophys. J.* **2009**, *97*, 1013–1021. [CrossRef]
9. Koch, T.M.; Münster, S.; Bonakdar, N.; Butler, J.P.; Fabry, B. 3D traction forces in cancer cell invasion. *PLoS ONE* **2012**, *7*, e33476. [CrossRef]

10. Liu, C.; Li, M.; Dong, Z.X.; Jiang, D.; Li, X.; Lin, S.; Chen, D.; Zou, X.; Zhang, X.D.; Luker, G.D. Heterogeneous microenvironmental stiffness regulates pro-metastatic functions of breast cancer cells. *Acta Biomater.* **2021**, *131*, 326–340. [CrossRef]
11. Houk, A.R.; Jilkine, A.; Mejean, C.O.; Boltyanskiy, R.; Dufresne, E.R.; Angenent, S.B.; Altschuler, S.J.; Wu, L.F.; Weiner, O.D. Membrane tension maintains cell polarity by confining signals to the leading edge during neutrophil migration. *Cell* **2012**, *148*, 175–188. [CrossRef] [PubMed]
12. Guilak, F.; Tedrow, J.R.; Burgkart, R. Viscoelastic properties of the cell nucleus. *Biochem. Biophys. Res. Commun.* **2000**, *269*, 781–786. [CrossRef] [PubMed]
13. Nava, A.; Mazza, E.; Furrer, M.; Villiger, P.; Reinhart, W.H. In vivo mechanical characterization of human liver. *Med. Image Anal.* **2008**, *12*, 203–216. [CrossRef] [PubMed]
14. González-Bermúdz, B.; Guinea, G.V.; Plaza, G.R. Advances in micropipette aspiration: Applications in cell biomechanics, models, and extended studies. *Biophys. J.* **2019**, *116*, 587–594. [CrossRef] [PubMed]
15. Weaver, W.M.; Tseng, P.; Kunze, A.; Masaeli, M.; Chung, A.J.; Dudani, J.S.; Kittur, H.; Kulkarni, R.P.; Carlo, D.D. Advances in high-throughput single-cell microtechnologies. *Curr. Opin. Biotechnol.* **2014**, *25*, 114–123. [CrossRef]
16. Crick, F.H.C.; Hughes, A.F.W. The physical properties of cytoplasm Part I. *Exp. Cell Res.* **1950**, *1*, 37–80. [CrossRef]
17. Smith, S.B.; Finzi, L.; Bustamante, C. Direct mechanical measurements of the elasticity of single DNA molecules by using magnetic beads. *Science* **1992**, *258*, 1122–1126. [CrossRef]
18. Sarkar, R.; Rybenkov, V.V. A guide to magnetic tweezers and their applications. *Front. Phys.* **2016**, *4*, 48. [CrossRef]
19. Mierke, C.T.; Puder, S.; Aermes, C.; Fischer, T.; Kunschmann, T. Effect of PAK inhibition on cell mechanics depends on Rac1. Front. *Cell Dev. Biol.* **2020**, *8*, 13. [CrossRef]
20. Adhikari, A.S.; Chai, J.; Dunn, A.R. Mechanical load induces a 100-fold increase in the rate of collagen proteolysis by MMP-1. *J. Am. Chem. Soc.* **2011**, *133*, 1686–1689. [CrossRef]
21. Hörber, J.K.H.; Miles, M.J. Scanning Probe Evolutionin Biology. *Science.* **2003**, *302*, 1002–1005. [CrossRef]
22. Dao, M.; Lim, C.T.; Suresh, S. Mechanics of the human red blood cell deformed by optical tweezers. *J. Mech. Phys. Solids.* **2003**, *51*, 2259–2280. [CrossRef]
23. Zhang, H.; Liu, K.K. Optical tweezers for single cells. *J. R. Soc. Interface* **2008**, *5*, 671–690. [CrossRef]
24. Dufrêne, Y.F.; Ando, T.; Garcia, R.; Alsteens, D.; Martinez-Martin, D.; Engel, A.; Gerber, C.; Müller, D.J. Imaging modes of atomic force microscopy for application in molecular and cell biology. *Nat. Nanotechnol.* **2017**, *12*, 295–307. [CrossRef]
25. Dufrêne, Y.F.; Pelling, A.E. Force nanoscopy of cell mechanics and cell adhesion. *Nanoscale* **2013**, *5*, 4094–4104. [CrossRef]
26. Lêvy, R.; Maaloum, M. Measuring the spring constant of atomic force microscope cantilevers: Thermal fluctuations and other methods. *Nanotechnology* **2002**, *13*, 33–37. [CrossRef]
27. Plodinec, M.; Loparic, M.; Monnier, C.A.; Obermann, E.C.; Zanetti-Dallenbach, R.; Oertle, P.; Hyotyla, J.T.; Aebi, U.; Bentires-Alj, M.; Lim, R.Y.; et al. The nanomechanical signature of breast cancer. *Nat. Nanotechnol.* **2012**, *7*, 757. [CrossRef] [PubMed]
28. Beshay, P.E.; Cortes-Medina, M.G.; Menyhert, M.M.; Song, J.W. The biophysics of cancer: Emerging insights from micro- and nanoscale tools. *Adv. Nanobiomed. Res.* **2022**, *2*, 2100056. [CrossRef] [PubMed]
29. Claudon, M.; Tranquart, F.; Evans, D.H.; Lefevre, F.; Correas, J.M. Advances in ultrasound. *Eur. Radiol.* **2002**, *12*, 7–18. [CrossRef]
30. Kirby, M.A.; Zhou, K.; Pitre, J.J., Jr.; Gao, L.; Li, D.; Pelivanov, I.; Song, S.; Li, C.; Huang, Z.; Shen, T.; et al. Spatial resolution in dynamic optical coherence elastography. *J. Biomed. Opt.* **2019**, *24*, 096006. [CrossRef]
31. Kikuchi, S.; Mikami, K.; Nakashima, D.; Kitamura, T.; Hasegawa, N.; Nishikino, M.; Kanaji, A.; Nakamura, M.; Nagura, T. Laser resonance frequency analysis: A novel measurement approach to evaluate acetabular cup stability during surgery. *Sensors* **2019**, *19*, 4876. [CrossRef] [PubMed]
32. Nakashima, D.; Mikami, K.; Kikuchi, S.; Nishikino, M.; Kitamura, T.; Hasegawa, N.; Matsumoto, M.; Nakamura, M.; Nagura, T. Laser resonance frequency analysis of pedicle screw stability: A cadaveric model bone study. *J. Ortho. Res.* **2021**, *39*, 2474–2484. [CrossRef] [PubMed]
33. Mikami, K.; Nakashima, D.; Kikuchi, S.; Kitamura, T.; Hasegqawa, N.; Nagura, T.; Nishikino, M. Stability diagnosis of orthopedic implants based on resonance frequency analysis with fiber transmission of nanosecond laser pulse and acceleration sensor. *Proc. SPIE* **2020**, *11233*, 112330. [CrossRef]
34. Kurahashi, S.; Mikami, K.; Kitamura, T.; Hasegawa, N.; Okada, H.; Kondo, S.; Nishikino, M.; Kawachi, T.; Shimada, Y. Demonstration of 25-Hz-inspection-speed laser remote sensing for internal concrete defects. *J. Appl. Remote Sens.* **2018**, *12*, 15009. [CrossRef]
35. Mikami, K.; Hasegawa, N.; Kitamura, T.; Okada, H.; Kondo, S.; Nishikino, M. Characterization of laser-induced vibration on concrete surface toward highly efficient laser remote sensing. *Jpn. J. Appl. Phys.* **2020**, *59*, 076502. [CrossRef]
36. Basoli, F.; Giannitelli, S.M.; Gori, M.; Mozetic, P.; Bonfanti, A.; Trombetta, M.; Rainer, A. Biomechanical characterization at the cell scale: Present and prospects. *Front. Physiol.* **2018**, *9*, 1449. [CrossRef]
37. Wu, J.R. Acoustic tweezers. *Acoust. J. Soc. Am.* **1991**, *89*, 2140. [CrossRef]
38. Wu, J.R.; Du, G.H. Acoustic radiation force on a small compressible sphere in a focused beam. *J. Acoust. Soc. Am.* **1990**, *87*, 997–1003. [CrossRef]
39. Lim, H.G.; Liu, H.C.; Yoon, C.W.; Jung, H.; Kim, M.G.; Yoon, C.; Kim, H.H.; Shung, K.K. Investigation of cell mechanics using single-beam acoustic tweezers as a versatile tool for the diagnosis and treatment of highly invasive breast cancer cell lines: An in vitro study. *Microsyst. Nanoeng.* **2020**, *6*, 39. [CrossRef]

40. Maslov, K.; Zhang, H.F.; Hu, S.; Wang, L.V. Optical-resolution photoacoustic microscopy for in vivo imaging of single capillaries. *Opt. Lett.* **2008**, *33*, 929–931. [CrossRef]
41. Wang, Y.; Hu, S.; Maslov, K.; Zhang, Y.; Xia, Y.; Wang, L.V. In vivo integrated photoacoustic and confocal microscopy of hemoglobin oxygen saturation and oxygen partial pressure. *Opt. Lett.* **2011**, *36*, 1029–1031. [CrossRef] [PubMed]
42. Mikami, K.; Zhao, Y.; Morita, M.; Sakamoto, T.; Nishikawa, H. Highly sensitive low-energy laser sensing based on sweep pulse excitation for bolt loosening diagnosis. *J. NDE* **2021**, *40*, 12. [CrossRef]
43. Mikami, K.; Sudo, N.; Okamoto, Y.; Nagura, T.; Nakashima, D. Sweep pulse excitation method for enhancing photoacoustic elastic waves at different laser irradiation parameters. *Sensors* **2022**, *22*, 5025. [CrossRef] [PubMed]
44. Sokolov, I.; Dokukin, M.E.; Kalaparthi, V.; Miljkovic, M.; Wang, A.; Seigne, J.D.; Grivas, P.; Demidenko, E. Noninvasive diagnostic imaging using machine-learning analysis of nanoresolution images of cell surfaces: Detection of bladder cancer. *Proc. Natl. Acad. Sci. USA* **2018**, *115*, 12920. [CrossRef]
45. Litjens, G.; Kooi, T.; Bejnordi, B.E.; Setio, A.A.A.; Ciompi, F.; Ghafoorian, M.; Laak, J.A.W.M.; Gonnelen, B.; Sánchez, C.I. A survey on deep learning in medical image analysis. *Med. Image Anal.* **2017**, *42*, 60–88. [CrossRef]
46. Sibille, L.; Seifert, R.; Avramovic, N.; Vebren, T.; Spottiswoode, B.; Zueblsdorff, S.; Schäfers, M. ^{18}F-FDG PET/CT uptake classification in lymphoma and lung cancer by using deep convolutional neural networks. *Radiology* **2020**, *294*, 445–452. [CrossRef]
47. Hrizi, O.; Gasmi, K.; Ltaifa, I.B.; Alshammari, H.; Karamti, H.; Krinchen, M.; Ammar, L.B.; Mahmood, M.A. Tuberculosis disease diagnosis based on an optimized machine learning model. *J. Healthc. Eng.* **2022**, *8950243*. [CrossRef]
48. Nemoto, M.; Tanaka, A.; Kaida, H.; Kimura, Y.; Nagaoka, T.; Yamada, T.; Hanaoka, K.; Kitajima, K.; Tsuchitani, T.; Ishii, K. Automatic detection of primary and metastatic lesions on cervicothoracic region and whole-body bone using a uniform machine-learnable approach for [18F]-FDG-PET/CT image analysis. *Phys. Med. Biol.* **2022**, *67*, 195013. [CrossRef]
49. Matsubara, K.; Ibaraki, M.; Nemoto, M.; Watabe, H.; Kimura, Y. A review on AI in PET imaging. *Ann. Neclear Med.* **2022**, *36*, 133–143. [CrossRef]
50. Nagaoka, T.; Kozuka, T.; Yamada, T.; Habe, H.; Nemoto, M.; Tada, M.; Abe, K.; Handa, H.; Yoshida, H.; Ishii, K.; et al. A deep learning system to diagnose COVID-19 pneumonia using masked lung CT images to avoid AI-generated COVID-19 diagnoses that include data outside the lungs. *Adv. Biomech. Eng.* **2022**, *11*, 76–86. [CrossRef]
51. Egorov, V.I.; Schastlivtsev, I.V.; Prut, E.V.; Baranov, A.O.; Turusov, R.A. Mechanical properties of the human gastrointestinal tract. *J. Biomech.* **2002**, *35*, 1417–1425. [CrossRef] [PubMed]
52. Mikami, K.; Nemoto, M.; Nagura, T.; Nakamura, M.; Matsumoto, M.; Nakashima, D. Machine learning-based diagnosis in laser resonance frequency analysis for implant stability of orthopedic pedicle screws. *Sensors* **2021**, *21*, 7553. [CrossRef] [PubMed]
53. Vapnik, V. Pattern Recognition using generalized portrait method. *Autom. Remote Control* **1963**, *24*, 774–780.
54. Bernhard, E.B.; Isabelle, M.G.; Vladimir, N.V. A training algorithm for optimal margin classifiers. In Proceedings of the Fifth annual Workshop on Computational Learning Theory (COLT '92). Association for Computing Machinery, New York, NY, USA, 27–29 July 1992; pp. 144–152.